Received 14 March 2021; accepted 2 April 2021. Date of publication 14 April 2021; date of current version 27 April 2021.

Digital Object Identifier 10.1109/OJAP.2021.3073104

Electronically Pattern Reconfigurable Antenna for IoT Applications

LUCA SANTAMARIA (Student Member, IEEE), FABIEN FERRERO (Member, IEEE), ROBERT STARAJ (Member, IEEE), AND LEONARDO LIZZI (Senior Member, IEEE)

Université Côte d'Azur, CNRS, LEAT, 06100 Nice, France

CORRESPONDING AUTHOR: L. LIZZI (e-mail: leonardo.lizzi@univ-cotedazur.fr)

This work was supported by the French Government, through the UCAJEDI Investments in the Future Project managed by the National Research Agency (ANR) with the reference number ANR-15-IDEX-0001.

ABSTRACT In this paper, an electronically pattern reconfigurable antenna for Internet of Things (IoT) applications is presented. The antenna consists of 4 wire-patches sharing the same ground plane. This radiating element can switch between four end-fire radiation states in less than 5 us and achieves a 290 MHz frequency bandwidth from 2.25 to 2.54 GHz. The results show that this antenna can realize a peak gain of 3.9 dBi at 2.44 GHz and a front-to-back ratio greater than 6.5 dB. A single low-power, low-insertion loss SP4T switch enables the radiation pattern steering. This approach avoids the use of multiple electronic components in the reconfiguration mechanism, thus accommodating the IoT microcontroller's limited resource constraints. The antenna structure is compact and printed on two cost-effective FR-4 printed circuit boards (PCBs). Thanks to its high performance, small size, low cost, and low-power characteristics, the proposed structure is suitable for IoT applications.

INDEX TERMS Pattern reconfigurable antennas, pattern agile antennas, wire-patch antennas, compact antennas, Internet of Things (IoT).

I. INTRODUCTION

INTERNET of Things (IoT) provides seamless interoperability between a large variety of low-power wireless devices via the Internet. Smart objects are continuously sensing the changes and gathering data from the environment. As reported in [1], the number of connected objects worldwide is expected to reach 29.3 billion by 2023. Large-scale IoT networks are characterized by massive volume of data, stringent resource constraints, and heterogeneous activity levels. The high number of communication links creates packet collision and decreases the overall network efficiency. Moreover, retransmitting packets raises node power usage despite their typically limited energy resources. In this scenario, pattern-reconfigurable antennas can filter the interference by targeting the radiation pattern towards a specific direction and decrease the data collisions rate, the average energy for packet transmission, and the latency opportunistically. Nodes equipped with switched beam antennas would allow 88% lower energy consumption and 24% lower data collision than a solution based on omnidirectional antennas [2]. Reconfigurable radiation patterns with maximal gain in the azimuth plane are usually preferred for long range communication.

Antenna reconfigurability can be achieved by controlling mechanical, physical, or optical switches. Among them, electronic switches are the most popular because of their efficiency and easy integration with microwave circuits. Radio Frequency (RF PIN diodes and RF MEMS are typical components used to achieve dynamic tuning. PIN diodes have some disadvantages, like a high insertion loss and lower efficiency [3]. However, the lower costs make them attractive amongst researchers. RF MEMS switches are near-zero power consumption. They offer miniaturization with no loss of functionality, fast actuation techniques, very low insertion loss, and extremely linear. Even though MEMS have only a few drawbacks, such as the need for costly transformers to provide high DC-bias voltages (40 V to 100 V), they are still difficult to integrate on PCB and they are still expensive [4]. In contrast, Gallium Arsenide (GaAs) and CMOS switches are relatively low cost and easy to integrate with RF circuitry. GaAs switches are small, they consume low power, and they have very good switching speed performance. They

are relatively low cost and easy to integrate into the antenna structure. Finally, the limited number of external components makes the interaction between the switch and the antenna kept to a minimum [5]–[7]. However, GaAs switches require DC blocking caps on RF inputs, an external driver, and are usually high-power (≥ 1 μA), making them unsuitable for power-constrained performance. CMOS switches are specifically designed to operate on a band of frequency up to 900 MHz. They can handle transmitted power up to 16 dBm. The low insertion loss, the high isolation between ports, the low distortion, and the low current consumption (1 μA max.) make these switches an excellent solution for low-power IoT applications [8], [9].

One possible solution to obtain radiation pattern reconfiguration relies on the use of parasitic element antenna arrays. These systems are constituted by a single driven radiator and multiple parasitic elements excited through the coupling effect. The overall radiation pattern is usually reconfigured by properly controlling variable loads connected to the parasitic elements [10]. However, in these solutions, each reactance's value needs to be controlled separately and is affected by the microcontroller output voltage variations. Other methods use integrated devices such as PIN diodes [11], [12], or dimmers [13] that can be turned on using external voltages. In [14], by changing the eight PIN diodes-based switches' states, the antenna provides eight pattern-reconfigurable modes. In [15], the proposed antenna achieves beam agility by reconfiguring parasitic striplines with 20 PIN diodes. While effective, all these reconfigurable design schemes are based on the use of several electronic components that do not fit the limited energy and computational resources usually available on autonomous IoT nodes.

In [16], a 3-D parasitic layer-based antenna changes its geometry using switches, thus providing reconfigurability of the radiation pattern in both the azimuth and vertical planes. However, the complex three-dimensional structure makes the antenna challenging to fabricate and integrate into an IoT device. In [17], a compact monopole antenna array with pairs of switchable parasitic strips is proposed. The introduction of control circuits in the antenna structure allows the realization of eight beams in the azimuth plane. However, this solution requires integration between the main steering elements with other discrete components, such as DC blocks or RF bypass components, to efficiently activate the reconfiguration circuit.

In this paper, a novel pattern reconfigurable antenna suitable for IoT applications is presented. A proof-of-concept of the antenna was proposed in [18]. The antenna structure is composed of 4 wire-patch antennas and operates in the 2.4 GHz band. The radiating elements and the control circuit are printed on two different FR4 printed circuit boards (PCBs), thus facilitating the integration into an IoT device. Each pattern configuration is activated using a single 0.45 dB insertion loss single-pole four-throw (SP4T) switch. The radiation structure is optimized to provide a maximum gain in the azimuth plane. The simple reconfiguration mechanism, the small size, and the low-cost realization make the proposed solution an ideal candidate to fulfill the demand for IoT systems with spatial filtering capabilities.

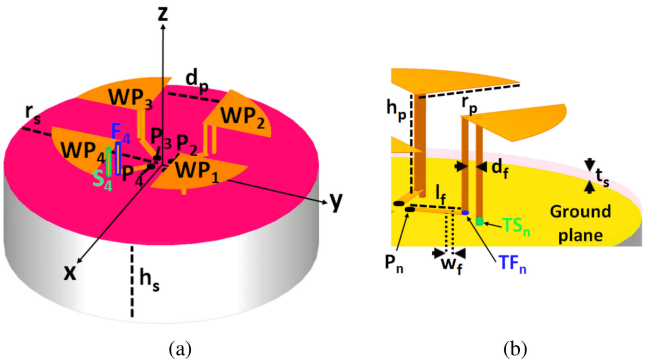

FIGURE 1. Initial antenna model: (a) 3-D isometric view and (b) zoom on the wire patch elements.

II. ANTENNA DESIGN

A. ANTENNA STRUCTURE

The proposed antenna geometry is shown in Fig. 1. It incorporates two layers, separated by an air gap. The top layer consists of a metal film that includes $N = 4$ fan-shaped microstrip patches while the bottom layer is a double side circular PCB. On one side of the board, the transmission lines used to feed the 4 antenna elements are printed. On the other side, a copper floor acts as a ground plane for the antenna. Each radiator is indicated with WP_n, $n = 1, \ldots, N$. The bottom PCB is printed on low-cost 0.8 mm thick FR-4 copper-cladded substrate with a relative dielectric permittivity of $\epsilon_r = 4.3$, a dielectric loss tangent of tan $\delta = 0.025$, and copper cladding thicknes of 0.035 mm.

Each patch is shorted to the ground plane by a copper pin S_n, whose termination is indicated by TS_n. The shorting pin is 8.835 mm long with a diameter of 0.5 mm. Each patch on the top copper film is connected to a second vertical wire marked as the feeding pin and indicated by F_n. The feeding pin height is indicated by h_p, and its diameter is 0.5 mm. The combination of the fan-shaped patch, the feeding pin and the shorting pin realizes a wire-patch radiating element. The feeding pins are connected through the pads TF_n to N microstrip lines printed on the bottom board. The microstrip lines are used to transfer the RF energy from a 50Ω discrete port to the 4 patches. The length and width of the microstrip lines are indicated by l_f and w_f, respectively. The distance between shorting and feeding pins is indicated by d_f.

A conductive skirt of height h_s has been placed under the lower PCB. The skirt surrounds the ground plane's circumference forming an empty cylinder connected along the edge of the copper floor. The ground skirting increases the ground plane's electrical length without changing its radius and it reduces the tilt in the elevation plane of the radiation pattern when the ground-plane size is limited [19], [20]. As a consequence the peak gain in the azimuth plane increases by reducing the elevation of the main lobe.

TABLE 1. Radiation states provided by the antenna.

State	φ_n [deg.]	P_1	P_2	P_3	P_4
A_1	225	fed	open	open	open
A_2	315	open	fed	open	open
A_3	45	open	open	fed	open
A_4	135	open	open	open	fed

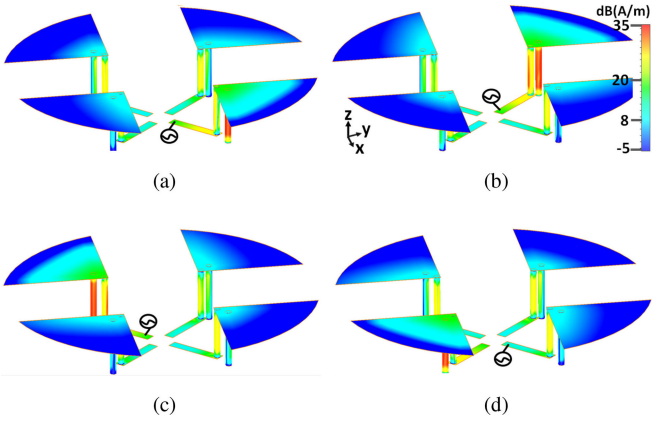

FIGURE 2. Current distribution on the antenna at 2.44 GHz. (a) A_1, (b) A_2, (c) A_3, and (d) A_4 antenna states.

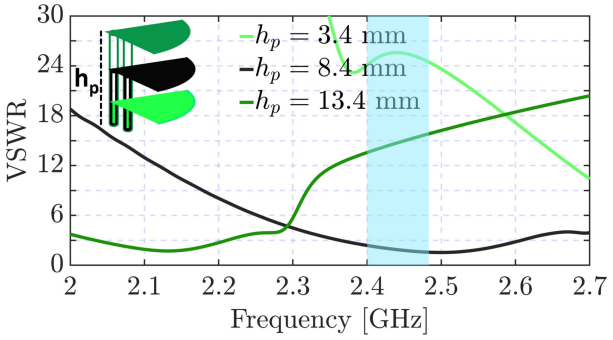

FIGURE 3. Effect of varying the patch height h_p (antenna in A_1 state).

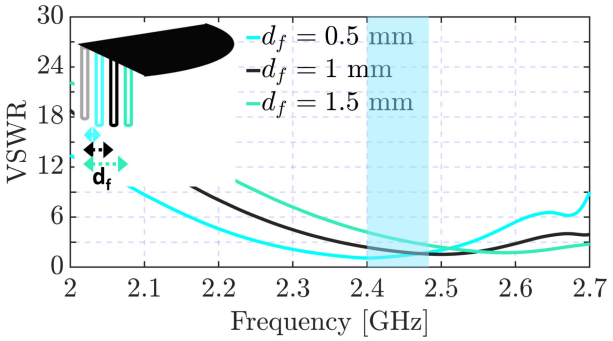

FIGURE 4. Effect of varying the distance d_f between the feeding wire and the short circuit (antenna in A_1 state).

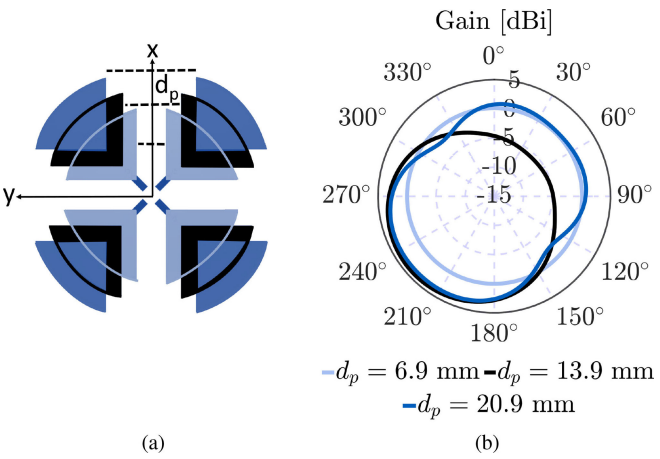

FIGURE 5. Effect of varying the distance d_p between each radiating unit. (a) Antenna model, (b) and realized gain pattern in the A_1 state for 3 different values of d_p.

B. ANTENNA RECONFIGURATION STATES

The reconfiguration mechanism of the antenna relies on the activation of one wire-patch radiating element at the time. The antenna can therefore provide $N = 4$ different states A_n, $n = 1, \ldots, N$. In each A_n state, the n-th 50-Ohm port injects the RF signal to the TF_n termination through the respective microstrip line, making the WP_n wire-patch active. The remaining ports P_k, $k = 1, \ldots, N$, $k \neq n$ are left in open circuit, so that all WP_k become parasitic elements and act as directors for WP_n. The antenna's main beam direction is determined by the phase differences between the driven and the parasitic elements. These latter contribute to the overall radiation of the antenna through the coupling mechanism. In this sense, the antenna is not the simple switchable combination of four wire-patch antennas, which would, otherwise, exhibit their classical omnidirectional radiation behavior. The proposed antenna can steer its main beam in the azimuth plane to N different directions φ_n with a discrete step of 90 degrees (see Table 1).

Fig. 2 illustrates the simulated surface current distribution at 2.44 GHz for each antenna state A_n. The strong current concentration on the standing pins distinguishes the antenna operating mode, which provides a vertically polarized radiation pattern. The inductances of both feeding and short-circuit wires act, together with the capacitance constituted by the fan-shaped patch and the ground plane, as a resonant circuit. The inductances are used to balance the antenna impedance matching [21], and the resulting equivalent circuit enables the TM_{01} mode of wire-patch antennas [22]. A change in patch height or size would therefore affect the resonant frequency of the antenna. Fig. 3 shows the effect of changing the patch height on the Voltage Standing Wave Ratio (VSWR) of the antenna. As expected, as the patch height decreases, the antenna resonant frequency increases.

Fig. 4 shows VSWR of the antenna in A_1 state for different values of d_f. As expected, the impedance matching can be tuned by modifying the distance between the feeding wire and the short circuit. More specifically, the VSWR lowers as the short circuit gets closer to the feed. When $d_f = 1$ mm, the resonance is centered at 2.44 GHz, and the matching achieves a VSWR lower than 2.4 in the operating band. It must be pointed out that, dealing with compact antennas, A

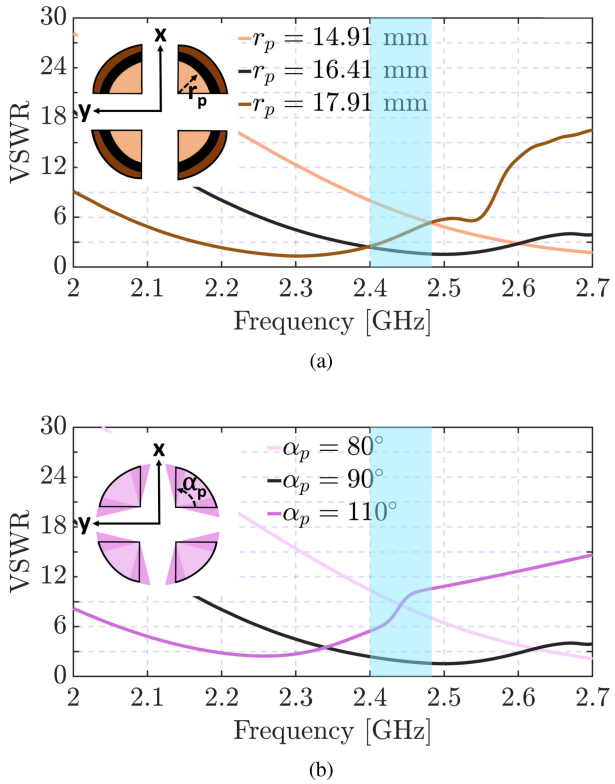

FIGURE 6. Effect of varying the patch dimension. Analysis of (a) the radius r_p, (b) and the angular aperture α_p (antenna in A_1 state).

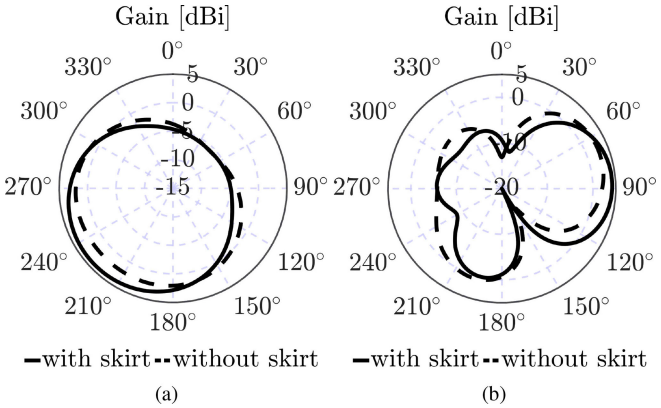

FIGURE 7. Simulated total realized gain patterns in the A_1 configuration with and without the conductive skirt in (a) the azimuth plane ($\theta = 90°$), and (b) the elevation plane at φ_1.

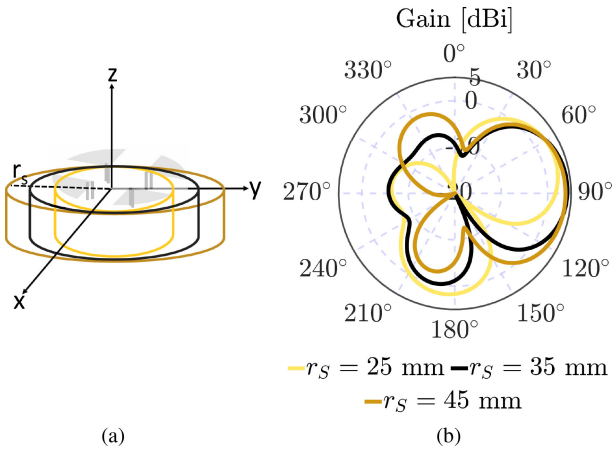

FIGURE 8. Effect of varying the skirt's diameter. (a) Antenna model, (b) and realized gain pattern in the A_1 state for 3 different values of the diameter of the skirt r_S.

VSWR lower than 3 is considered to be acceptable for IoT applications [23]–[26], since, as the antenna gets smaller, it becomes harder to have a matching with a high Q-factor. Moreover, given the low transmission powers of IoT devices, the losses due to a VSWR = 3 lead to a signal level reduction that is not noticeable over the air (if compared with the signal level when the antenna has a lower VSWR, e.g., equal to 1.92).

Fig. 6 shows the effect of changing the radius r_p and the angular apertures α_p of each wire-patch for the same antenna state. The figure reveals that the antenna resonant frequency is determined by both the angle and radius of the radiating unit. As expected, the antenna resonance decreases as the radius of the patch increases [see Fig. 6(a)], whereas it increases as the angular aperture of the fan-shaped patch element decreases [see Fig. 6(b)]. For $r_p = 16.41$ mm and $\alpha_p = 90°$, the antenna can cover 240 MHz from 2.36 to 2.6 GHz with a VSWR ≤ 3. It is worth noting that the variation of the antenna resonance provided by the modification of the patch height (please see Fig. 3) is more important than the one caused by the patch dimension. For this reason, we have first optimized the patch height and then the patch size.

The separation between each radiating element has been determined to optimize the radiation performance of the antenna in the state A_1. The distance between the elements must be sufficient to ensure a good gain. On the other hand, such distance must not be too large so that the mutual coupling can be properly exploited to obtain the desired radiation behavior (minimum backward radiation and increased front-to-back ratio), as shown in Fig. 5.

In order to clarify the role of the conductive skirt, the simulated realized gain patterns provided by the antenna in the A_1 configuration with (solid line) and without (dashed line) the skirt are shown in Fig. 7. Fig. 7(b) clearly illustrates that, when the skirt is not present, the maximum of radiation is directed at $\theta = 69°$ (21 degrees off the azimuth plane). The maximum realized gain in the horizontal plane is 1.99 dBi, i.e., 2.21 dBi lower than the gain obtained with the skirt [see Fig. 7(a)].

In order to clarify how the height and diameter of the skirt have been selected, the antenna radiation performance has been evaluated in the A_1 state for the different antenna models shown in Figs. 8(a) and 9(a). The simulated realized gain patterns in the elevation plane for different values of the skirt's height and diameter are shown in Figs. 8(b) and 9(b), respectively. As it can be noticed, the selected skirt diameter is the smallest one that provides the maximum of radiation in the horizontal plane without any tilt in the elevation plane [see Fig. 8(b)]. Similarly, Fig. 9(b) shows that the selected

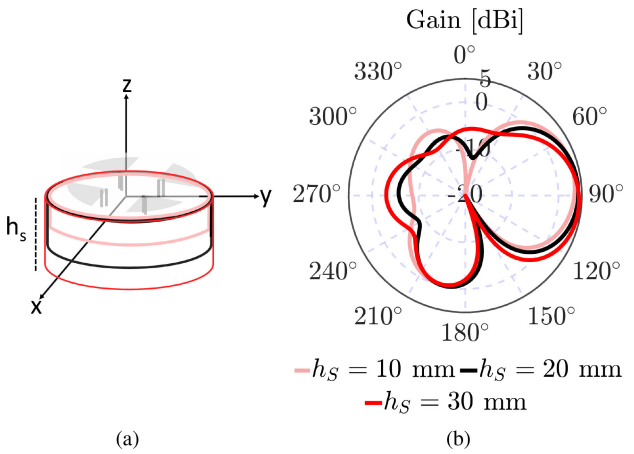

FIGURE 9. Effect of varying the skirt's height. (a) Antenna model, (b) and realized gain pattern in the A_1 state for 3 different values of the height of the skirt h_S.

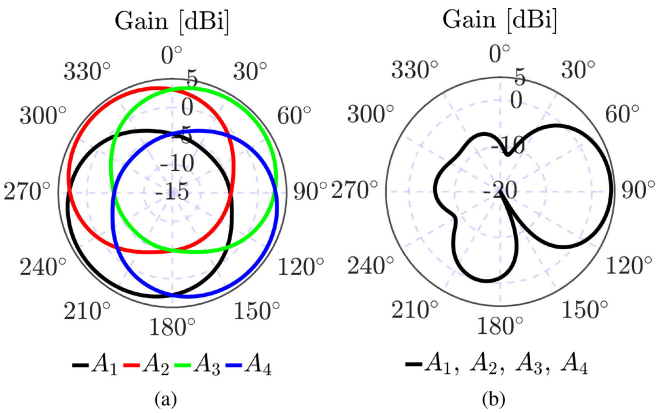

FIGURE 10. The different radiation pattern configurations provided by the antenna. The patterns represent the total realized gain in (a) the azimuth plane ($\theta = 90°$), and (b) the elevation plane at φ_n, $n = 1 \cdots N$.

skirt height is the one that puts the maximum of radiation in the horizontal plane. When the skirt height is smaller or larger, the maximum tilts towards $\theta < 90°$ or $\theta > 90°$.

Finally, the realized gain of the antenna in its 4 antenna states at 2.44 GHz is shown in Fig. 10. As it can be observed, the patterns have a constant angular spacing of 90° and the antenna is capable of providing 360-degree coverage in the principal plane cut at $\theta = 90°$ [see Fig. 10(a)]. The peak realized gain in the direction of maximum radiation is almost 4.2 dBi. The half-power beamwidth (HPBW) of each pattern is about 135° with a minimum gain between two consecutive patterns of 3.1 dBi. Moreover, each pattern has a high front-to-back ratio (FBR) of more than 9 dB, which can help in spatial filtering of interfering signals coming from the backward direction. For completeness, the radiation patterns in the vertical planes at the different φ_n (see Table 1) are shown in Fig. 10(b). Because of the antenna symmetry, the vertical cuts look exactly the same.

C. RECONFIGURATION CIRCUIT IMPLEMENTATION

A reconfigurable network based on a SP4T switch is implemented to accomplish the reconfiguration of the radiation

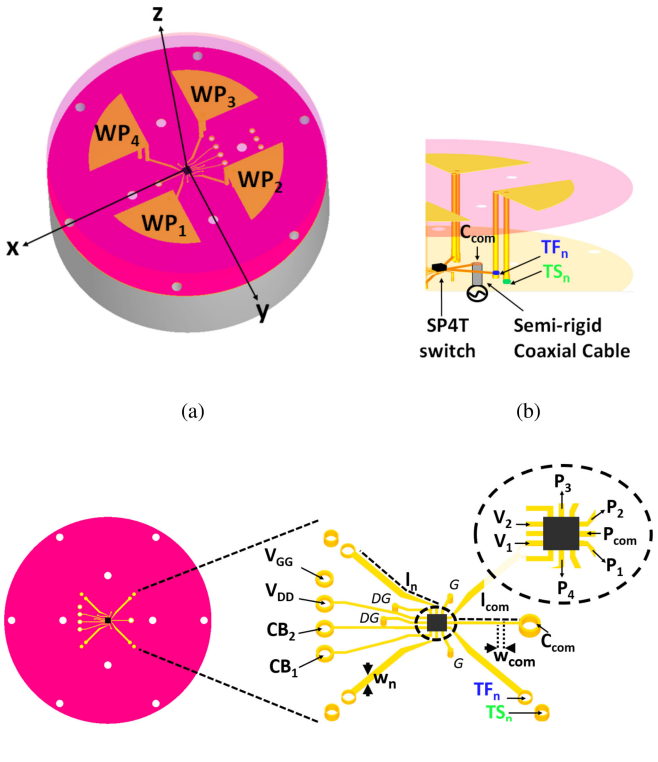

FIGURE 11. Final antenna structure: (a) 3-D isometric view, (b) zoom on the wire-patch, (c) bottom PCB including the SP4T switch and the reconfiguration circuit.

pattern. The numerical model of the antenna structure including the reconfiguration circuit is shown in Fig. 11. The copper film on the top layer is now printed on a FR-4 dielectric substrate that makes the antenna more rigid and easy to integrate into an IoT device. The 4 wire-patch radiators share a single DC control circuit. This results in savings power resources of the IoT node, which are usually limited (e.g., when the node is battery powered). The switching network is placed on the bottom PCB to limit the impact on the radiation performance when the reconfiguration is activated. The selected SP4T switch is the PE613050 SP4T from Peregrine, which is a CMOS-based tuning control switch with low on-resistance and insertion loss. Both decoding and biasing are integrated on-chip with the two-pin low voltage control. There is no need for external DC filtering or biasing components to prevent the DC and RF current's short circuit. The switch is characterized by 0.45 dB of insertion loss and a very low-on resistance of $R = 1.6\ \Omega$ at 2.44 GHz. For low-power IoT services, a CMOS switch represents the most suitable means of reconfiguration amongst the many popular electronic switches proposed in literature. It is worth noting that the SP4T switch allows 4 directive radiation states that can satisfy the 360-deg coverage with a power consumption of 1 μA, which is approximately 10000 times lower than the typical current value (10 mA) required to control PIN diodes [27].

Fig. 11(c) shows the schematic of the DC bias lines to control the SP4T switch. The switch input port is named

TABLE 2. Optimized parameters of the proposed antenna.

Parameter	Size [mm]	Parameter	Size [mm]
r_p	16.41	d_p	13.9
r_s	35	l_{com}	9.09
l_f	9.1	w_{com}	0.25
w_f	1.55	l_1	9.09
h_p	8.4	l_2	8.84
d_f	1	l_3	9.09
t_s	0.8	l_4	8.84
h_s	20	w_n	0.6

P_{com}, while the four outputs are indicated with $P_n, n = 1, \ldots, N$. Each output port is connected to the respective feeding pin F_n via the pad TF_n.

The RF signal is injected from a 50 Ω coaxial cable through the pad C_{com} and then to the input port of the switch P_{com} via a transmission line of dimension l_{com} and w_{com}. One output port of the switch is always in the ON state, and the other three are in the OFF state. The SP4T is used to practically activate one of four antenna configuration. When the A_n antenna mode is selected, the switch allows the transfer of the RF signal from the coaxial cable to TF_n and thus to the n-th wire-patch antenna element. The PE613050 switch relies on open reflective unselected ports characterized by a very high reflection coefficient. Thus the remaining output ports P_k, $k = 1, \ldots, N$, $k \neq n$ are left in an open circuit mode. Each transmission line used to route the RF signal from F_n to TF_n has been designed using a coplanar waveguide (CPW) model using a trace of length l_n, initial width w_n, and metal thickness of 0.035 mm. The RF output pads of the SP4T switch are thinner than the 50 Ω lines. In order to connect each output switch port P_n to the feeding pin F_n of the radiating unit, the width w_n have been tapered to a reasonable degree. This increases the RF current injected in the connecting lines and avoids step discontinuities that cause VSWR mismatch. Starting from the dimension of a standard isolated 50 Ω line, the width of w_n and w_{com} lines have been optimized separately to obtain the best insertion loss considering the available space and the integration constraints. This resulted in two different line widths.

The paths that link the RF input port to the selected RF output ports are modeled as an equivalent circuit composed of a parallel connection of a fixed capacitor $C = 0.14$ pF and a variable resistor R_n. In each antenna state A_n, $R_n = 1.6$ Ω (low-on resistance) so that P_n is in ON, while $R_k = 400$ kΩ, $k = 1, \ldots, N$, $k \neq n$ (P_k OFF). The switch requires only two voltage control bits to enable the four antenna configurations. The switch pads V_1 and V_2 receives the control voltages and put each output port P_n either in low or high-impedance state. G and DG indicate respectively, the ground and digital ground. The optimized values of the final antenna model's geometric parameters, as well as the values of the reconfiguration circuit layout, are listed in Table 2.

III. NUMERICAL AND EXPERIMENTAL RESULTS

The optimized pattern-reconfigurable antenna has been fabricated and tested. Fig. 12 shows the pre-assembly prototype

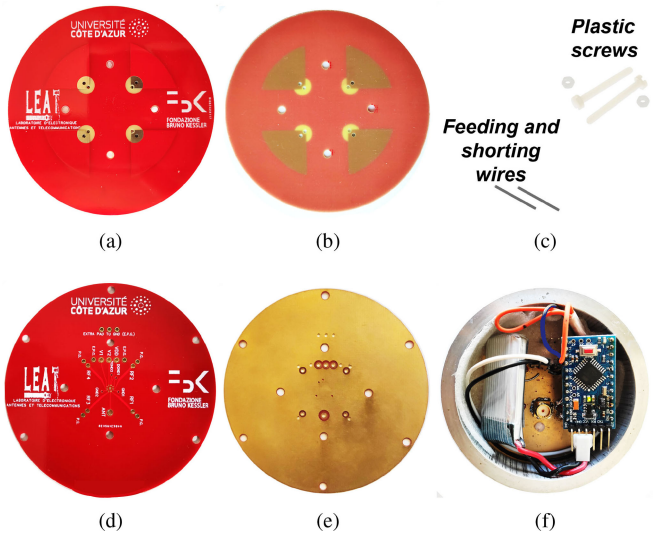

FIGURE 12. Antenna prototype. Pre-assembly antenna elements: (a)-(b) top and bottom view of the top PCB, (c) vertical metallic pins and plastic screws, (d)-(e) top and bottom view of the bottom PCB, and (f) integration of the RF and DC stages.

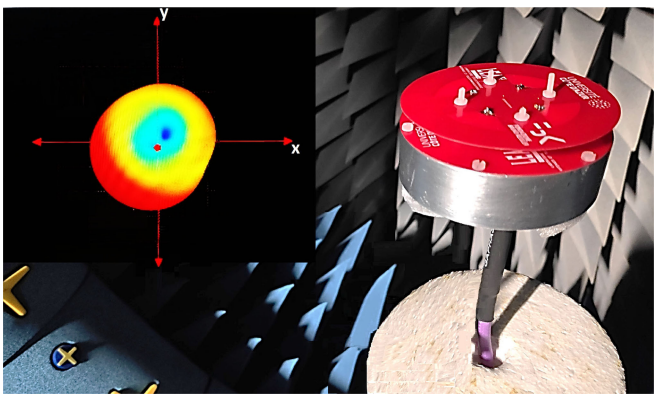

FIGURE 13. Assembled antenna. 3-D radiation pattern and antenna under test (AUT) measurement test setup.

elements of the antenna. Figs. 12(a), (b), (d), (e) show the top and bottom faces of the two PCBs. The plastic screws of Fig. 12(c) support the top PCB and keep it at the correct distance of 8.4 mm from the bottom PCB. The metallic wires have been used as feeding and shorting pins. The antenna allows suitable integration of the RF and DC electronic stages thanks to its natural protection created by the skirt and the bottom PCB's ground plane. The integration of the RF and DC electronic stages is shown in Fig. 12(f). The material of the skirt is an aluminum-manganese alloy. The alloy offers good strength and turns the skirt into natural protection to the antenna's RF and DC electronic stages accommodated inside it. The alloy allows the skirt to be easily soldered with the bottom layer's copper film to which it is attached and has good conductivity ($\sigma = 3.5 \times 10^7$ S/m). On the bottom face of the lower PCB, the prototype has been equipped with a classical SMA connector to inject the RF signals and with wires soldered to the pads of the switching circuit. These electrical wires are connected to an Arduino

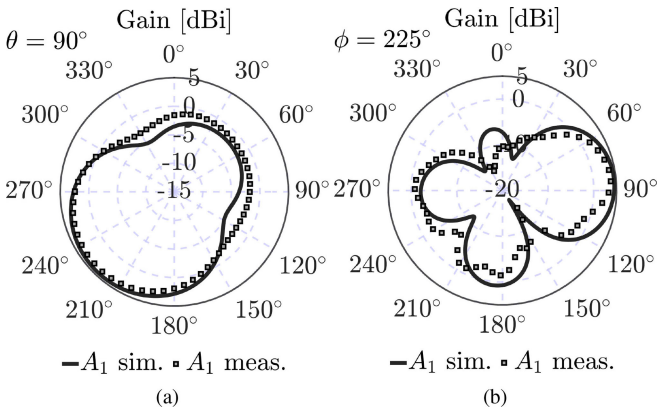

FIGURE 14. Simulated and measured realized gain patterns of the antenna in the A_1 state.

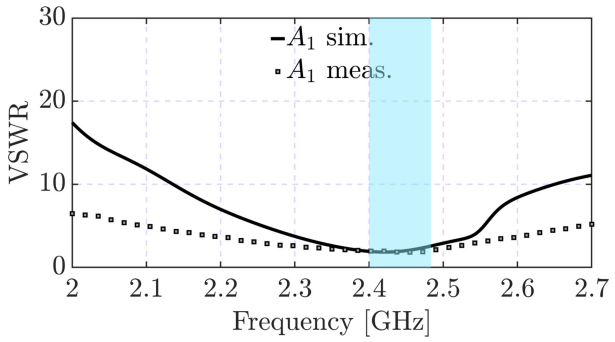

FIGURE 15. Simulated and measured VSWR of the antenna in the A_1 state.

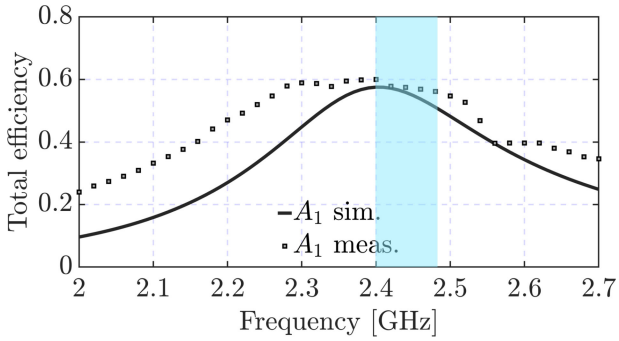

FIGURE 16. Simulated and measured total efficiency of the antenna in the A_1 state.

Pro Mini powered by a 3.3 V battery. The Arduino provides the DC supply voltage to the switch through the V_{DD} pad and the voltage control bits through the CB_1 and CB_2 pads (see Fig. 11). Finally, the microcontroller and antenna grounds are connected through the V_{GG} pad. Both the electric and radiating characteristics of the prototype have been tested in a Satimo Starlab Station. Because of the symmetry of the antenna structure, only the results of the antenna state A_1 are here reported. Fig. 14 shows the simulated (solid line) and measured (dotted line) realized gain values in the horizontal and vertical planes. As it can be noticed, numerical and experimental data are in good agreement. The simulated and measured maximum realized gains are 4.45 dBi and 3.9 dBi, respectively. The measured main-beam is pointed to 230° (225° in simulation) in the horizontal plane with a 80° half-power beamwidth (HPBW) from 190° to 270° (a 115° HPBW from 167° to 282° in simulation). The side lobe pointing at $\theta = 180°$ is mainly due to the limited dimensions of the antenna ground plane. As shown in Fig. 8, when the antenna ground plane increases, the side lobe intensity in the vertical direction decreases. However, to keep the antenna size as small as possible, a smaller skirt radius has been selected (the minimum one for which the maximum of radiation was in the horizontal plane). It must be pointed out that, since IoT network nodes are usually considered to be communicating in the same horizontal plane, having a side lobe in the vertical direction will not increase the interference level. The antenna exhibits a measured FBR higher than 6.5 dB. This value is acceptable in the majority of IoT applications. As demonstrated in [16], the spatial filtering capability given by a pattern reconfigurable antenna with a FBR approaching 7 dB provides up to 29% of network capacity gain and 13% coverage improvement compared to the standard case in which a legacy omnidirectional antenna is used.

Fig. 15 shows the simulated and measured VSWR of the antenna over frequency. It can be seen that the antenna achieves a measured impedance bandwidth of 290 MHz ranges from 2.25 to 2.54 GHz with a VSWR ≤ 3. These data are in good agreement with the numerical ones. The simulated antenna impedance bandwidth covers 170 MHz from 2.33 GHz to 2.5 GHz. The differences between the simulated and measured VSWR values outside the band of interest can be ascribed to the currents flowing on the coaxial cable used to feed the antenna during the measurement phase. These currents increase the electrical size of the antenna ground plane, resulting in a decrease of the antenna Q-factor and therefore in an increase of the impedance bandwidth.

Finally, the simulated and measured antenna total efficiency is depicted in Fig. 16. The measure results well fit the simulated ones, especially in the band of interest, confirming the effectiveness of the antenna numerical model. The differences in terms of quality factor can be ascribed to imperfections in the realization of the prototype. The measured antenna total efficiency varies between to 57% and 60% in the 2.4 GHz band.

Table 3 presents the characteristics of the proposed solution compared with those of other works available in literature. The solutions in [12], [15], [16] have static power consumptions higher than the power handling capabilities of standard IoT receivers (usually 30 mW). In our solution, a monolithically integrated tuning solution based on CMOS technology reduces the overall power consumption, which is only 0.42 mW, less than the power consumption of the solutions presented in [10]–[12], [15]–[17]. Only in [13], single pole single throw (SPST) switches have been used to activate the reconfiguration with a lower static power consumption (0.0013 mW). However the 4 radiation patterns that are enabled have a maximum gain of only 1.5 dBi in

TABLE 3. Comparison to the state of the art.

Reference	Fabrication cost and S.C.* complexity [Low/High]	Steering elements	Number of components in the S.C.	S.C. static power consumption [mW]	Number of radiation states	Size	N. of radiation states / N. of components in the S.C.	Gain at $\theta = 90°$ / largest dimension [1/λ]
[10]	Low	DTC	3	0.5	3	$0.48\lambda_0 \times 0.07\lambda_0$	1	6.16
[11]	Low	PIN diodes	24	25	8	$0.65\lambda_0 \times 0.56\lambda_0$	0.33	4.53
[12]	High	PIN diodes	36	600	6	$2.5\lambda_0 \times 0.5\lambda_0$	0.16	0.4
[13]	High	SPST switches	8	0.0013	4	$1.23\lambda_0 \times 0.028\lambda_0$	0.5	1.14
[14]	Low	PIN diodes	32	N.A.	8	$0.74\lambda_0 \times 0.12\lambda_0$	0.25	1.35
[15]	High	PIN diodes	30	161.5	5	$0.57\lambda_0 \times 0.28\lambda_0$	0.16	5.15
[16]	High	PIN diodes	15	66.5	7	$0.57\lambda_0 \times 0.38\lambda_0$	0.46	4.22
[17]	High	PIN diodes	44	1.8	8	$1\lambda_0 \times 0.1\lambda_0$	0.18	1
Our work	**Low**	**SP4T switch**	**1**	**0.42**	**4**	$\mathbf{0.23}\lambda_0 \times \mathbf{0.56}\lambda_0$	**4**	**4.6**

* S.C.= switching circuitry

the azimuth plane which is less than the peak gain offered by the proposed solution (3.9 dBi).

Moreover, Table 3 shows that a ratio between the number of radiation states and the number of reconfigurable components of the proposed antenna is equal to 4, which is higher than the ratio obtained by the solutions in [11], [12], [14]–[17]. Using a single switch to reconfigure the radiation pattern eliminates the use of many circuit modules and, consequently, it well fits the microcontroller's limited resource constraints. An acceptable ratio of the number of the states over the number of components equal to 1 is obtained in [10]. However, the microcontroller's output voltage variations affect the capacitance values provided by the DTC, which also needs to be independently controlled. Finally, the solutions presented in [10], [15] have a larger ratio between the antenna realized gain in the principal cut $\theta = 90°$ and its largest dimension when compared with the antenna proposed here. However, the solution in [10] is based on a differential antenna, and the lack of a ground plane makes the development and the integration with radio-frequency circuitry difficult. Besides, the gain performance of [15] relies on expensive substrate and complex biasing network. Instead, the proposed antenna solution is printed on two cost-effective FR-4 PCBs suitable for massive production.

IV. CONCLUSION

A novel pattern reconfigurable antenna suitable for IoT applications has been presented in this paper. The antenna structure consists of only two FR4 PCBs, vias, and a metallic skirt, making the antenna easy to realize and cheap to produce. The antenna can steer its radiation pattern to four overlapping endfire directions in the azimuth plane. The reconfiguration of the pattern is activated using a single low insertion loss, low on-resistance SP4T switch controlled by a 2-bit microcontroller-generated voltage combination. Its simple reconfiguration mechanism, limited volume, and low-cost realization make the proposed antenna an ideal candidate to satisfy the need of IoT devices with spatial filtering capabilities.

ACKNOWLEDGMENT

The authors would like to thank Elisabetta Farella and his research group at the Bruno Kessler Foundation (FBK), Trento, Italy, for the helpful discussion about the use of pattern reconfigurable antennas in IoT localization applications. CREMANT is acknowledged for support on measurements.

REFERENCES

[1] "Cisco annual Internet report (2018–2023)," Cisco, San Jose, CA, USA, White Paper, vol. 1, pp. 1–35, 2020.

[2] T. N. Le, A. Pegatoquet, T. Le Huy, L. Lizzi, and F. Ferrero, "Improving energy efficiency of mobile WSN using reconfigurable directional antennas," *IEEE Commun. Lett.*, vol. 20, no. 6, pp. 1243–1246, Jun. 2016.

[3] F. A. Asadallah, J. Costantine, and Y. Tawk, "A multiband compact reconfigurable PIFA based on nested slots," *IEEE Antennas Wireless Propag. Lett.*, vol. 17, pp. 331–334, 2018.

[4] M. D. Wright, W. Baron, J. Miller, J. Tuss, D. Zeppettella, and M. Ali, "MEMS reconfigurable broadband patch antenna for conformal applications," *IEEE Trans. Antennas Propag.*, vol. 66, no. 6, pp. 2770–2778, Jun. 2018.

[5] T. Aboufoul, A. Alomainy, and C. Parini, "Reconfiguring UWB monopole antenna for cognitive radio applications using GaAs FET switches," *IEEE Antennas Wireless Propag. Lett.*, vol. 11, pp. 392–394, 2012.

[6] H. L. Lee, D. H. Park, and M. Q. Lee, "A reconfigurable directional coupler using a variable impedance mismatch reflector for high isolation," *J. Electromagn. Eng. Sci.*, vol. 16, no. 4, pp. 206–209, 2016.

[7] X.-L. Yang, J.-C. Lin, G. Chen, and F.-L. Kong, "Frequency reconfigurable antenna for wireless communications using GaAs FET switch," *IEEE Antennas Wireless Propag. Lett.*, vol. 14, pp. 807–810, 2015.

[8] H. Wang *et al.*, "Small-size reconfigurable loop antenna for mobile phone applications," *IEEE Access*, vol. 4, pp. 5179–5186, 2016.

[9] L. Santamaria, T. Q. K. Nguyen, F. Ferrero, R. Staraj, and L. Lizzi, "Flexible reconfigurable antenna robust to folding in wearable applications," in *Proc. IEEE Int. Symp. Antennas Propag. USNC-URSI Radio Sci. Meeting*, Atlanta, GA, USA, 2019, pp. 1–2.

[10] L. Lizzi *et al.*, "Differential pattern-reconfigurable antenna prototype for efficient wireless sensor networks," in *Proc. IEEE Int, Symp. Antennas Propag. (APSURSI)*, Fajardo, PR, USA, 2016, pp. 1239–1240.
[11] M. Burtowy, M. Rzymowski, and L. Kulas, "Low-profile ESPAR antenna for RSS-based DoA estimation in IoT applications," *IEEE Access*, vol. 7, pp. 17403–17411, 2019.
[12] Y. Yang and X. Zhu, "A wideband reconfigurable antenna with 360° beam steering for 802.11ac WLAN applications," *IEEE Trans. Antennas Propag.*, vol. 66, no. 2, pp. 600–608, Feb. 2018.
[13] L. Akhoondzadeh-Asl, J. J. Laurin, and A. Mirkamali, "A novel low-profile monopole antenna with beam switching capabilities," *IEEE Trans. Antennas Propag.*, vol. 62, no. 3, pp. 1212–1220, Mar. 2014.
[14] Y.-Y. Bai, S. Xiao, M.-C. Tang, C. Liu, and B.-Z. Wang, "Pattern reconfigurable antenna with wide angle coverage," *Electron. Lett.*, vol. 47, no. 21, pp. 1163–1164, Oct. 2011.
[15] S.-L. Chen, P.-Y. Qin, W. Lin, and Y. J. Guo, "Pattern-reconfigurable antenna with five switchable beams in elevation plane," *IEEE Antennas Wireless Propag. Lett.*, vol. 17, pp. 454–457, 2018.
[16] M. A. Hossain, I. Bahceci, and B. A. Cetiner, "Parasitic layer-based radiation pattern reconfigurable antenna for 5G communications," *IEEE Trans. Antennas Propag.*, vol. 65, no. 12, pp. 6444–6452, Dec. 2017.
[17] Y. Juan, W. Che, W. Yang, and Z. N. Chen, "Compact pattern-reconfigurable monopole antenna using parasitic strips," *IEEE Antennas Wireless Propag. Lett.*, vol. 16, pp. 557–560, 2017.
[18] L. Santamaria, L. Lizzi, F. Ferrero, and R. Staraj, "Compact 4-element radiation pattern agile antenna for spatial filtering in IoT networks," in *Proc. 14th Eur. Conf. Antennas Propag. (EuCAP)*, Copenhague, Denmark, Mar. 2020, pp. 1–4.
[19] D. V. Thiel, "Tin-can antenna—A switched parasitic monopole antenna on a finite ground plane with a conductive sleeve," in *Proc. CSIRO 7th Aust. Symp. Antennas*, 2001, p. 19.
[20] Y. Gao, C. C. Chiau, X. Chen, and C. G. Parini, "Modified PIFA and its array for MIMO terminals," *IEEE Proc. Microw. Antennas Propag.*, vol. 152, no. 4, pp. 255–259, Aug. 2005.
[21] D. Schaubert, F. Farrar, A. Sindoris, and S. Hayes, "Microstrip antennas with frequency agility and polarization diversity," *IEEE Trans. Antennas Propag.*, vol. 29, no. 1, pp. 118–123, Jan. 1981.
[22] C. Delaveaud, P. Leveque, and B. Jecko, "New kind of microstrip antenna: The monopolar wire-patch antenna," *Electron. Lett.*, vol. 30, no. 1, pp. 1–2, Jan. 1994.
[23] W. Luo, W. Chen, Y. Feng, and Y. Yang, "A novel automobile antenna for vehicles communication of IoT systems in 5G network," *EURASIP J. Wireless Commun. Netw.*, vol. 2020, p. 218, Oct. 2020.
[24] J. M. Floch, B. El Jaafari, and A. E. S. Ahmed, "New compact broadband GSM/UMTS/LTE antenna realised by 3D printing," in *Proc. Int. Symp. 9th Eur. Conf. Antennas Propag. (EuCAP)*, Lisbon, Portugal, 2015, pp. 1–4.
[25] M. Donelli, S. Menon, and A. Kumar, "Compact antennas for modern communication systems," *Int. J. Antennas Propag.*, vol. 2020, pp. 1–2, Feb. 2020.
[26] C. H. Friedman, "Wide-band matching of a small disk-loaded monopole," *IEEE Trans. Antennas Propag.*, vol. 33, no. 10, pp. 1142–1148, Oct. 1985.
[27] L. Santamaria, F. Ferrero, R. Staraj, and L. Lizzi, "Slot-based pattern reconfigurable ESPAR antenna for IoT applications," *IEEE Trans. Antennas Propag.*, early access, Dec. 22, 2020, doi: 10.1109/TAP.2020.3044399.

LUCA SANTAMARIA (Student Member, IEEE) received the first M.Sc. degree in computer science from the Université Côte d'Azur, Sophia Antipolis, France, and the second M.Sc. degree in telecommunications engineering from the Politecnico di Bari, Bari, Italy, in 2018. He is currently pursuing the Ph.D. degree with the Laboratory of Electronics, Antennas, and Telecommunications, Université Côte d'Azur. At the moment, his research focuses on the development of miniature and low-power reconfigurable antenna systems for future Internet-of-Things networks.

FABIEN FERRERO (Member, IEEE) received the Ph.D. degree in electrical engineering from the University of Nice-Sophia Antipolis in 2007. From 2008 to 2009, he worked for IMRA Europe, Aisin Seiki Research Center as a Research Engineer and developed automotive antennas. In 2010, he is recruited as an Associate Professor with the Polytechnic School, Université Nice Sophia-Antipolis. Since 2018, he has been a Full Professor with the Université Côte d'Azur. He is doing his research with the Laboratoire d'Electronique, Antennes et Telecommunications. His studies concerned the design and measurement of millimetric antennas, IoT systems, and reconfigurable antennas.

ROBERT STARAJ (Member, IEEE) was born in Antibes, France, in 1965. He received the Ph.D. degree in electronics from University Nice-Sophia Antipolis, France, in 1992. In 1993, he joined the ESINSA Engineering School (École Supérieure d'Ingénieurs de Nice-Sophia Antipolis) and the Laboratory of Electronics, Antennas and Télécommunications-CNRS UMR7248 (LEAT), as an Assistant Professor. Since 2003, he has been a Full Professor with Polytech'Nice-Sophia, École Polytechnique de l'Université de Nice-Sophia, and an In-Charge of the Telecommunications and Networks speciality of the Electronics Department. He has been the Director of the GDR Ondes-CNRS, French National Research Group on Waves from 2014 to 2017, and an Assistant Director of the LEAT. After being the head of CMA Research Group, Conception et Modélisation d'Antennes—Antennas Design and Modeling, LEAT during several years, he is currently the Director of LEAT. His research focuses on printed antennas and arrays, active, integrated, adaptative, and miniature multistandard antennas for wireless, RFID, MIMO systems, and biomedical applications.

LEONARDO LIZZI (Senior Member, IEEE) received the M.Sc. degree in telecommunication engineering and the Ph.D. degree in information and communication technology from the University of Trento, Italy, in 2007 and 2011, respectively. During his Ph.D. he has been a Visiting Researcher with Pennsylvania State University, USA, and the University of Nagasaki, Japan. From 2011 to 2014, he was a Postdoctoral Researcher with the Laboratory of Electronics, Antennas and Telecommunications, Université Côte d'Azur, Sophia Antipolis, France, where he has been Maître de Conférences (an Associated Professor) since 2014. At the moment, his research focuses on reconfigurable, miniature, multistandards antennas for Internet-of-Things applications, wearable devices, and 5G terminals.